AGU PUBLICATIONS

JGR

Journal of Geophysical Research: Space Physics

RESEARCH ARTICLE
10.1002/2016JA022777

This article is a companion to *Varney et al.* [2016] doi:10.1002/2016JA022778.

Key Points:
- We present a coupled geospace model including an ion outflow model with causally regulated ion acceleration by wave-particle interactions
- The numerical techniques conserve mass between the ionospheric and magnetospheric portions of the coupled model
- The free parameters in the outflow model can be tuned to yield plausible outflow distributions that agree with empirical relationships

Correspondence to:
R. H. Varney,
roger.varney@sri.com

Citation:
Varney, R. H., M. Wiltberger, B. Zhang, W. Lotko, and J. Lyon (2016), Influence of ion outflow in coupled geospace simulations: 1. Physics-based ion outflow model development and sensitivity study, *J. Geophys. Res. Space Physics*, *121*, 9671–9687, doi:10.1002/2016JA022777.

Received 31 MAR 2016
Accepted 14 AUG 2016
Accepted article online 16 SEP 2016
Published online 18 OCT 2016

Influence of ion outflow in coupled geospace simulations: 1. Physics-based ion outflow model development and sensitivity study

R. H. Varney[1], M. Wiltberger[2], B. Zhang[2], W. Lotko[3], and J. Lyon[4]

[1]Center for Geospace Studies, SRI International, Menlo Park, California, USA, [2]High Altitude Observatory, National Center for Atmospheric Research, Boulder, Colorado, USA, [3]Thayer School of Engineering, Dartmouth College, Hanover, New Hampshire, USA, [4]Department of Physics and Astronomy, Dartmouth College, Hanover, New Hampshire, USA

Abstract We describe a coupled geospace model that includes causally regulated ion outflow from a physics-based ionosphere/polar wind model. The model two-way couples the multifluid Lyon-Fedder-Mobarry magnetohydrodynamics (MHD) model to the ionosphere/polar wind model (IPWM). IPWM includes the H^+ and O^+ polar wind as well as a phenomenological treatment of energetic O^+ accelerated by wave-particle interactions (WPI). Alfvénic Poynting flux from the MHD simulation causally regulates the ion acceleration. The wave-particle interactions (WPI) model has been tuned and validated with comparisons to particle-in-cell simulations and empirical relationships derived from Fast Auroral Snapshot satellite data. IPWM captures many aspects of the ion outflow that empirical relationships miss. First, the entire coupled model conserves mass between the ionospheric and magnetospheric portions, meaning the amount of outflow produced is limited by realistic photochemistry in the ionosphere. Second, under intense driving conditions, the outflow becomes flux limited by what the ionosphere is capable of providing. Furthermore, the outflows produced exhibit realistic temporal and spatial delays relative to the magnetospheric energy inputs. The coupled model provides a flexible way to explore the impacts of dynamic heavy ion outflow on the coupled geospace system. Some of the example simulations presented exhibit internally driven sawtooth oscillations associated with the outflow, and the properties of these oscillations are analyzed further in a companion paper.

1. Introduction

Hydrodynamic theories of the ionosphere correctly predicted that light ions (H^+ and He^+) should escape gravity along open polar cap field lines and outflow at supersonic speeds into the magnetosphere [*Axford*, 1968; *Banks and Holzer*, 1969]. Satellite observations have incontrovertibly established existence and ubiquity of this "classical polar wind" [*Yau et al.*, 1985; *Abe et al.*, 1993a]. Nonetheless, the discovery of heavy O^+ ions in the magnetosphere by *Shelley et al.* [1972] was surprising since this ion is almost nonexistent in the solar wind, and classical polar wind theories predicted that these ions should remain gravitationally bound at all reasonable ionospheric temperatures. Decades of satellite observations have demonstrated that O^+ is often a major constituent of the magnetosphere (see *Kronberg et al.* [2014] for a review). The outflowing O^+ ions are often observed as either ion beams accelerated by parallel forces [*Shelley et al.*, 1976] or as ion conics resulting from transverse acceleration followed by mirror-force lifting [*Sharp et al.*, 1977]. These non-Maxwellian distributions indicate that wave-particle interactions and other kinetic processes are needed to understand heavy ion outflow. A variety of "nonclassical acceleration mechanisms" have been proposed to explain how some heavy ions are accelerated to escape velocities (see *Yau and André* [1997], *André and Yau* [1997], and *Yau et al.* [2011] for reviews).

Most of the nonclassical acceleration mechanisms operate primarily at high altitudes, and in order for ions to experience them they must first upflow from the topside ionosphere. Ion outflow is frequently discussed as a two-step process first involving deposition of energy at *F* region altitudes generating ion upflow followed by high-altitude acceleration converting upflow into outflow [*Strangeway et al.*, 2005]. Based on incoherent scatter radar observations, *Wahlund et al.* [1992] categorized ion upflow events into two classes. Type I upflows are associated with Joule heating and enhanced ion temperature. Type II upflows are associated with soft

precipitation, enhanced electron temperature, and enhanced ambipolar electric field. The typical pattern of ion parallel fluxes at ~840 km altitude is primarily upward over the dayside cusp and auroral oval and downward over the polar cap [*Loranc et al.*, 1991; *Coley et al.*, 2003; *Redmon et al.*, 2010].

Unlike the topside ionosphere, polar wind observations show that O^+ fluxes are always upward above 4000 km [*Abe et al.*, 1993a]. The typical hemispheric integrated outflow rates are on the order of 10^{26} ions/s [*Yau et al.*, 1985] with the value scaling exponentially with both geomagnetic activity and solar EUV flux [*Yau et al.*, 1988]. The quiet time distribution of outflow observed by the POLAR satellite at 6000 km shows that statistically the most O^+ outflow comes from the dayside cleft region, the second most comes from the nightside auroral oval near magnetic midnight, and relatively little comes from the polar cap [*Lennartsson et al.*, 2004; *Peterson et al.*, 2008]. A statistical study of distribution of ion outflow observed by the Fast Auroral Snapshot (FAST) spacecraft at 4000 km demonstrated a similar distribution [*Chaston et al.*, 2007]. The ions energized in the cleft convect poleward to form the "cleft ion fountain" [*Lockwood et al.*, 1985]. Statistical studies using FAST [*Strangeway et al.*, 2005] and POLAR [*Zheng et al.*, 2005] show significant correlations between outflows at 4000 and 6000 km, respectively, and various types of magnetospheric energy inputs.

The relationships between magnetospheric inputs and high-altitude acceleration remain poorly understood. The candidate mechanisms can be divided into parallel and transverse acceleration mechanisms. Convecting field lines will accelerate ions in the parallel direction due to the centrifugal force [*Cladis*, 1986], but this effect is small below 1 R_E altitude. Large parallel electric fields with potential drops over 1 keV develop on auroral field lines in regions of upward field-aligned current [*Knight*, 1973; *Fridman and Lemaire*, 1980]. These potential drops are more than sufficient to supply the 10 eV escape energy for O^+. These fields, however, tend to form above 5000 km in altitude [*Bennett et al.*, 1983]. Parallel ambipolar electric fields can be enhanced by photoelectrons [*Khazanov et al.*, 1997, 1998; *Glocer et al.*, 2012; *Varney et al.*, 2014] or secondary electrons at lower altitudes [*Glocer*, 2015; *Cohen et al.*, 2015], but the total potential associated with these fields is normally only a few volts.

Ion beams are rarely observed below 5000 km, so energetic ion observations at low altitudes are normally attributed to transverse acceleration mechanisms [*Yau and André*, 1997]. A frequently discussed mechanism is ion cyclotron resonance heating (ICRH) by waves that match the ion gyrofrequency [*Crew et al.*, 1990]. Statistical studies of Freja data from 1400 to 1700 km [*Norqvist et al.*, 1998; *Knudsen et al.*, 1998; *Hamrin et al.*, 2002] and FAST data from 2000 to 4000 km [*Lund et al.*, 2000] claim that ICRH by resonant waves within broadband extremely low frequency (BBELF) turbulence is the dominant transverse acceleration mechanism. In addition to ICRH, BBELF waves can also accelerate ions via nonresonant heating by multiple waves whose frequencies sum to the ion gyrofrequency [*Temerin and Roth*, 1986] and Landau interactions with waves whose phase velocity matches the ion velocities [*Chang and Coppi*, 1981]. These actions can be difficult to distinguish from each other during BBELF observations [*Knudsen et al.*, 1998]. *Norqvist et al.* [1998] concluded that BBELF could explain 90% of the O^+ heating observations and 95% of the total O^+ upflow flux. Despite these studies, the observational community still does not agree on the nature of BBELF and its importance in ion acceleration. Single-spacecraft measurements have inherent space-time ambiguities which complicate the interpretation of BBELF; for example, a spacecraft moving at 8 km/s cannot differentiate between waves at 10 Hz and 800 m horizontal structures. *Kintner et al.* [2000] used an interferometry technique to derive frequencies and wavelengths of BBELF from multiple-payload sounding rocket measurements and showed that the waves do not follow the dispersion relation of any known normal mode in a homogeneous plasma.

A number of alternative mechanisms for transverse ion acceleration mechanisms have been proposed. The Landau interaction condition can also be met by short-wavelength whistler/lower hybrid waves in the VLF range [*Knudsen et al.*, 1998; *Hamrin et al.*, 2002]. At much lower frequencies, dispersive Alfvén waves can transversely accelerate ions either coherently or stochastically depending on their perpendicular wave number [*Chaston et al.*, 2004]. Alfvén waves also accelerate ions in the parallel direction via ponderomotive forces [*Guglielmi and Lundin*, 2001]. Even constant perpendicular electric fields can produce non-Maxwellian ion distributions. *Moore and Khazanov* [2010] describe an ambipolar pickup process by which the relative motion between ionospheric ions and thermospheric neutrals can produce torodial ion velocity distributions.

Assessing the impact of heavy ions on magnetospheric dynamics has only recently become possible with the advent of multifluid global MHD models. *Wiltberger* [2015] gives a review of the approaches used by the Winglee model [*Winglee*, 1998], the multispecies and multifluid BATS-R-US models [*Glocer et al.*, 2009a, 2009b], and the multifluid Lyon-Fedder-Mobarry (MFLFM) model [*Wiltberger et al.*, 2010]. These three models use

similar formulations of the multifluid MHD equations but completely different methods for specifying ionospheric outflows at the models' inner boundaries. Nonetheless, the three groups have observed some common effects of heavy ion outflow. Adding ion outflow tends to reduce the cross polar cap potential [*Winglee et al.*, 2002; *Welling and Zaharia*, 2012], inflate the magnetosphere [*Brambles et al.*, 2010; *Welling and Zaharia*, 2012], increase the inner magnetospheric pressure and ring current [*Glocer et al.*, 2009a, 2009b; *Welling and Zaharia*, 2012], move the tail reconnection X line tailward [*Brambles et al.*, 2010; *García et al.*, 2010; *Yu and Ridley*, 2013], and decrease the dayside reconnection rates [*Zhang et al.*, 2016b]. The addition of extra ion outflow can sometimes lead to additional substorms that would not appear in a single-fluid simulation, depending on where the outflow lands in the tail [*Wiltberger et al.*, 2010; *Yu and Ridley*, 2013]. Heavy ions in the tail also provide an explanation for the formation of earthward moving plasmoids [*Zhang et al.*, 2016a].

Methods for specifying ion outflow in a global MHD model can be divided into noncausal and causal methods. The simplest type of noncausal approach is to specify patches of constant ion outflow flux from fixed locations [e.g., *Wiltberger et al.*, 2010; *García et al.*, 2010; *Yu and Ridley*, 2013]. These studies suggest that the impact of an ion outflow population is highly sensitive to the location and velocity of the outflow since these determine whether the ions will enter the plasma sheet or be lost down tail.

Models employing causal specifications of ion outflow have the possibility of creating magnetosphere-ionosphere feedback loops. The early multifluid MHD studies performed by *Winglee* [1998] used a passive inner boundary where constant densities are placed in the ghost cells in the inner boundary and pressure gradients, centrifugal forces, and numerical diffusion pull this density into the computational domain. *Welling and Liemohn* [2014] demonstrated that the default boundary conditions in the BATS-R-US produce outflow in this manner as well and that this "de facto outflow" causally responds to the intensity of solar wind driving in the model. A more sophisticated way to causally specify outflow is to two-way couple a physics-based ion outflow model to a global MHD model. The first model to do this was the two-way coupling of the Polar Wind Outflow Model (PWOM), a classical polar wind model, and BATS-R-US [*Glocer et al.*, 2009a, 2009b]. *Welling et al.* [2015] demonstrated that this model exhibits a positive feedback loop where electron heating from region 2 currents enhances the PWOM outflows, enhances the inner magnetospheric pressure, and further enhances the region 2 currents. Another way to create causal outflow is to use empirical relationships between outflow and magnetospheric energy inputs. *Brambles et al.* [2010] drove the MFLFM with an empirical relationship between the DC Poynting flux and O^+ ion outflow flux determined from FAST data [*Strangeway et al.*, 2005]. The empirical relationship only gives the number flux, so to fully specify the MHD inner boundary conditions assumptions need to be made about the ion velocities and temperatures. Another empirical approach was created by *Garcia-Sage et al.* [2015] who combined the DC Poynting flux and auroral precipitation relationships from FAST [*Strangeway et al.*, 2005] with an empirical model of the thermal polar wind from Akebono [*Ebihara et al.*, 2006]. *Brambles et al.* [2011] introduced a different empirical relationship, also determined from FAST data, using the Alfvénic Poynting flux instead. Simulations using that empirical relationship were the first to develop internally driven sawtooth oscillations associated with the ion outflow [*Brambles et al.*, 2011, 2013; *Ouellette et al.*, 2013].

The purpose of this paper is to develop a physically motivated ion outflow modeling technique that can be used to introduce dynamic and causally regulated ion outflow into a global geospace model while capturing effects that empirical models miss. A central design objective for the model is to conserve mass between the ionospheric and magnetospheric portions such that the outflow is always limited by realistic ionospheric photochemistry. Empirical outflow models create mass at the inner boundary of an MHD model without any regard for what the ionosphere is capable of providing. *Varney et al.* [2015] presented the ionosphere/polar wind model (IPWM) and its phenomenological treatment of ion energization by wave-particle interactions. This paper extends that work by coupling IPWM into a global modeling framework. Section 2 describes the constituent models and their coupling. In order to generate significant amounts of heavy ion outflow, the model employs a parameterized treatment of ICRH by BBELF that is causally regulated by the incident Alfvénic Poynting flux from the magnetospheric MHD model. Section 3 describes the details of this treatment of WPI and validates our approach with comparisons to kinetic simulations. Section 4 shows example simulations using the coupled model, discusses the features of the outflow produced, and compares the results to previously used empirical relationships. Some of the simulations presented exhibit internally driven sawtooth oscillations, and a companion paper analyzes the mechanisms generating these features in detail. Section 5 contains concluding remarks.

2. Model Descriptions and Coupling Framework

The simulations presented here employ three coupled models: the multifluid Lyon-Fedder-Mobarry (MFLFM) model of magnetospheric MHD, the magnetosphere-ionosphere exchange (MIX) model of electron precipitation and high-latitude ionospheric electrostatics, and the ionosphere/polar wind model (IPWM) of high-latitude plasma transport. Sections 2.1–2.3 summarize the important features of these models, and section 2.4 describes the coupling between them.

2.1. Multifluid Lyon-Fedder-Mobarry Model

The Lyon-Fedder-Mobarry (LFM) model is a finite-volume, ideal MHD model that has been extensively used for magnetospheric studies [*Lyon et al.*, 2004]. The multifluid LFM (MFLFM) uses an extended equation set that solves for the densities, velocities, and temperatures of any number of ion species in the first-order drift approximation [*Wiltberger et al.*, 2010]. In this approximation the parallel ion velocities are independent, but all species drift perpendicular to **B** at the $\mathbf{E} \times \mathbf{B}$ velocity. The electron pressure is neglected since it is known to be relatively small compared to the ion pressures and magnetic pressure. This assumption removes the parallel ambipolar electric field and the possibility of electrostatic counterstreaming instabilities. Faraday's law is solved in the ideal MHD limit; nonetheless, the numerical dissipation in the code enables magnetic reconnection. *Ouellette et al.* [2013] performed detailed studies of tail reconnection in the MFLFM and showed that the reconnection electric fields scale as $0.1 v_A B_{in}$, where v_A and B_{in} are the inflowing Alfvén speed and magnetic field strength, respectively. This relationship holds over a range of X line positions in the tail despite the variation in the LFM grid, thus proving that the reconnection is controlled by the plasma parameters and not the numerical dissipation [see also *Fedder et al.*, 1995]. The addition of heavy ions reduces the Alfvén speed and thus slows the reconnection rates in the model, in agreement with the predictions of *Shay and Swisdak* [2004].

The MFLFM grid extends 30 R_E upstream, 300 R_E downstream, and 100 R_E outward in the SM *YZ* plane. The inner boundary is a sphere of radius $2R_E$. Like *Brambles et al.* [2011], the simulations presented here use the double-resolution grid. The grid is a warped spherical grid with 53 cells in the radial direction, and 48×64 cells in the angular directions. Near the inner boundary the radial sizes of cells are $0.5R_E$, and cells in the magnetotail map to approximately 200 to 300 km cells when projected along dipole field lines to 100 km altitude. Comparisons of these results to results performed on the quadruple-resolution grid ($106 \times 96 \times 128$) will be performed in a later study.

The upstream boundary conditions require a specification of the solar wind/interplanetary magnetic field (SW/IMF) conditions, and the sides and back of the model use Neumann outflow conditions. The default inner boundary conditions use a perfect hard wall. The four ghost cells are populated with antisymmetric copies of the densities and velocities in the first four active cells, which ensure that the reconstructed flux through the inner interface is always zero. This means that unlike the Winglee and BATS-R-US models, MFLFM will never produce any numerical outflow from the inner boundary. It also means that ions in the magnetosphere can never disappear into the inner boundary. MHD cannot describe magnetic mirror trapping, but the hard wall boundary condition performs the same phenomenological function and keeps the inner magnetosphere ions trapped.

2.2. Magnetosphere-Ionosphere Coupler

In order to set the electromagnetic inner boundary conditions, MFLFM relies on the magnetosphere-ionosphere coupler (MIX) model of ionospheric electrostatics [*Merkin and Lyon*, 2010]. MIX takes MHD state variables from the inner boundary as inputs. The MHD density and temperatures are used to estimate the electron density and temperature. The electron state variables and FAC are used with a Knight-Fridman-Lemaire formulation to predict the field-aligned potential drop, precipitating number flux, and precipitating particle energy [*Zhang et al.*, 2015]. Depending on whether the potential drop is greater or less than twice the inferred electron thermal energy, the model produces either monoenergetic or diffuse precipitation, respectively [*Zhang et al.*, 2015]. The version of MIX used in this study also includes two additional forms of soft electron precipitation. The first is broadband electron (BBE) precipitation which is regulated by the 5–180 s band-pass-filtered Alfvénic Poynting flux as described by *Zhang et al.* [2012]. This simulated Alfvénic Poynting flux is calculated using the electric and magnetic fields at grid cells near the inner boundary of the simulation as $S_{\parallel} = \delta\left(\delta\mathbf{E} \times \delta\mathbf{B}\right) \cdot \mathbf{B} / \left(\mu_0 B\right)$, where μ_0 is the permeability of free space. The band-pass-filtered perturbation fields $\delta\mathbf{E}$ and $\delta\mathbf{B}$ are "Alfvénic" in the sense that the ratio $\delta E_{\perp} / \delta B_{\perp}$ is usually consistent with the Alfvén

wave phase velocity in this pass band in LFM simulations. The Alfvénic Poynting flux is mapped to 100 km altitude along dipole field lines assuming $S_{||}/B$ is constant. The second additional form of precipitation is cusp direct entry precipitation. The location of the cusp is determined using the MHD density as described by *Zhang et al.* [2013]. These precipitation models were originally developed for the single-fluid LFM. For the present study we use the same models and only use the density and temperature of the solar wind fluid to determine the empirically and dynamically specified parameters of the precipitation model. Using the multispecies bulk parameters would create a nonphysical direct coupling between the outflows and the precipitation. Nonetheless, even when using the solar wind fluid the outflow still indirectly affects the precipitation since the outflow tends to exclude solar wind fluid from inner portions of the simulation domain. Further work on the empirical precipitation models for use in the MFLFM is still needed.

MIX uses empirical models to convert the precipitation parameters and solar EUV inputs into conductance distributions [*Robinson et al.*, 1987; *Wiltberger et al.*, 2009]. MIX solves two elliptic boundary value problems for the 2-D ionospheric potential in the two hemispheres for given distributions of FAC and conductance. The boundary conditions are zero potential at ±45° magnetic latitude. The potential is mapped up equipotential dipole field lines to the inner boundary of the MFLFM and used to set the electric fields and perpendicular velocities. When coupled to the double-resolution MFLFM, the default MIX resolution is a 2° ×2° magnetic latitude-longitude grid extending poleward from 45° latitude.

2.3. Ionosphere/Polar Wind Model

The ionosphere/polar wind model (IPWM) is a 3-D model of high-latitude plasma transport. The model solves eight-moment equations for the parallel transport of H^+, He^+, $O^+\left(^4S\right)$, and electrons. The model additionally includes the photochemistry of N^+, NO^+, N_2^+, O_2^+, $O^+\left(^2D\right)$, and $O^+\left(^2P\right)$. Details of the parallel transport and chemistry schemes are given by *Varney et al.* [2014]. The input neutral thermospheric parameters come from NRLMSISE-00 [*Picone et al.*, 2002], and the solar EUV spectrum comes from HUEVAC [*Richards et al.*, 2006]. Details of the perpendicular transport scheme and coupling to MIX are given by *Varney et al.* [2015]. Like the simulations from *Varney et al.* [2015], the kinetic electron solver is disabled. The production and heating by precipitation are determined by the empirical relationships from *Fang et al.* [2008].

IPWM employs an Eulerian, nonorthogonal grid constructed from surfaces of constant L shell, magnetic local time (MLT), and altitude. The lower boundary at 97 km is set by chemical equilibrium, and the upper boundary at 8400 km is open. The equatorward boundary at $L = 4$ (~60° magnetic latitude) is treated as a hard wall. The simulations presented here use 2° magnetic latitude resolution at 100 km, which matches the MIX latitude resolution. The MLT resolution varies moving inward toward the pole. The model encompasses a total of 513 magnetic flux tubes.

IPWM includes an extra fluid to model nonthermal O^+ that obeys a different set of transport equations from the other fluids. The model includes free parameters that are used to phenomenologically model WPI. *Varney et al.* [2015] presented demonstrations where WPI parameters were held fixed in a dayside heating region and the convection pattern varied. Even with the WPI parameters held constant, the properties of resultant cleft ion fountain varied as the convection varied since both the residence time in the heating region and the ion upflow flux generated by frictional heating depend on convection. The simulations presented in this work use a much more sophisticated method for regulating the WPI parameters as described in section 3.

2.4. Model Coupling

Figure 1 diagrams the coupling between the three models. The models run asynchronously and only communicate between each other once every 10 s of simulation time. The MFLFM and IPWM time steps are typically 0.08 and 0.4 s, respectively, and vary according to the Courant conditions in each model. Between exchange times, MFLFM and IPWM hold their respective inputs constant. MIX is a time-independent model that is only called once per exchange.

During an exchange, MFLFM first passes the FAC computed from $\nabla \times \mathbf{B}$, the solar wind fluid MHD densities and temperatures used for precipitation, and the band-pass-filtered Alfvénic Poynting flux to MIX. MIX then completes all of its work to compute precipitation, conductances, and the electrostatic potential. MIX passes the potential to both MFLFM and IPWM. MIX also passes the precipitating number fluxes and characteristic energies for all three type of precipitation (mono/diffuse, BBE, and cusp) and the Alfvénic Poynting flux to IPWM.

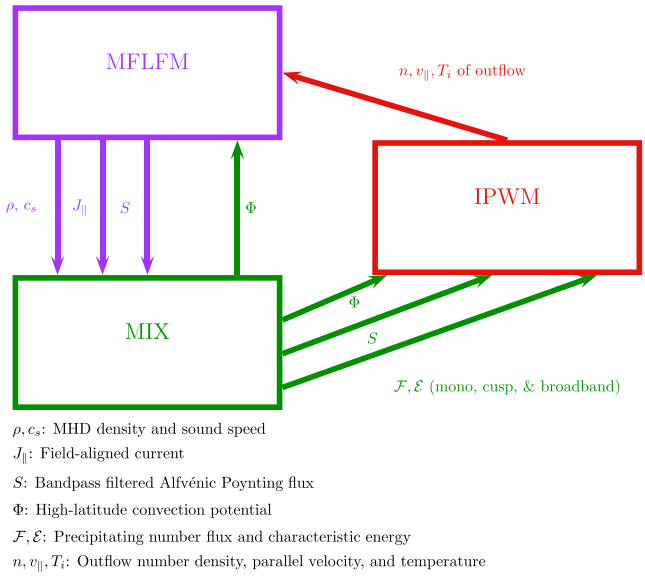

Figure 1. Diagram of the model coupling.

Lastly, during an exchange the IPWM passes the densities, velocities, and sound speeds of outflowing species to the MFLFM. The IPWM parameters are first interpolated to the location of the MFLFM inner boundary ($1R_E$ altitude) in their native representation in terms of density, momentum density, and energy density. Then the parameters are converted to density, velocity, and sound speed and interpolated to the MFLFM grid using bilinear interpolation in magnetic latitude and longitude. The IPWM and MFLFM grids are both Eulerian grids fixed with respect to SM coordinates, so the coefficients for this interpolation only need to be computed once. The IPWM has a 2000 km buffer between its open upper boundary at $\sim 2.3R_E$ and the MFLFM inner boundary. This ensures boundary effects in the IPWM do not impact the coupling.

The MFLFM uses the IPWM inputs to modify its inner boundary conditions on all fluids except the solar wind fluid. The MFLFM uses a symmetric, eight-cell stencil to reconstruct the fluxes at any interface. This means that the flux through the inner interface depends on the four ghost cells as well as the first four active cells. If the ghost cells are set according to the IPWM values the reconstructed flux at the interface would not necessarily match the IPWM outflow flux, leading to numerical creation or deletion of mass. Rather than modify the ghost cell values, the model directly manipulates the fluxes at the inner interface. This allows IPWM to inject outflow into the MFLFM domain without letting any ions already in the domain leak back out through the boundary. Direct modification of the flux in this way reduces the solver to first-order accuracy in the radial direction near the inner boundary, however. The MFLFM uses operator splitting to divide the work of each time step into several substeps. First, the ghost cell values are set according to the first four active cells. Then the hydrodynamic fluxes through each interface are reconstructed, and the hydrodynamic variables are updated. Then the Lorentz force calculation and magnetic field updates are done as subsequent steps. The modified code performs an extra step after the hydrodynamic update but before the Lorentz force and magnetic field updates. The extra mass fluxes, momentum fluxes, and energy fluxes through the inner interface are calculated from the IPWM outflow parameters, and the active cells adjacent to the inner interface are updated according to these extra fluxes. This procedure ensures that the rate at which plasma enters the MFLFM exactly equals the rate at which is leaves the IPWM to within grid-interpolation errors. Tests with patches of constant outflow using this inner boundary condition have confirmed that the mass of the outflow fluid in the MFLFM domain equals the specified flux multiplied by interval of time the flux was applied. The MFLFM inner boundary conditions do not conserve momentum and energy, however, so in order to prevent a significant mismatch between the IPWM outflow parameters and the MFLFM inner boundary parameters, the parallel velocities and the sound speeds at the active cell adjacent to the inner interface are overwritten with the IPWM values at the end of each complete time step.

Like the PWOM BATS-R-US coupling implemented by *Glocer et al.* [2009a], no direct communication from the MFLFM fluid variables back to the IPWM fluid variables is included. When the IPWM outflows are supersonic, no information should propagate downward, so this only causes problems for the subsonic cold O^+ population. The extra outflow driven by the ionosphere-magnetosphere pressure gradient is neglected. Flows of cold ions back down the field line are not permitted. If the IPWM velocity at the interface happens to be downward, it is set to zero before passing to the MFLFM. In practice, downward flows of cold ions at altitudes above 4000 km are rarely if ever observed [*Abe et al.*, 1993a]. A self-consistent treatment of the pressure gradient force across the boundary would be challenging to implement in a numerically stable way given the asynchronous nature of the coupling and the inconsistencies between the MFLFM and IPWM equations sets.

For the idealized simulations presented here, IPWM is only run for the Northern Hemisphere. When IPWM passes to MFLFM, hemispheric symmetry is assumed and the Northern Hemisphere values are copied into the Southern Hemisphere. This assumption is justified for simulations at equinox with no dipole tilt and no IMF B_x, IMF B_y, SW V_y, or SW V_z. Including hemispheric asymmetry will be explored as a later project. In the volume within $L = 4$, equatorward of the IPWM boundary, the outflow fluxes are set to zero. The MFLFM hard wall is maintained, so any plasma in this region cannot disappear into the inner boundary. Currently, no midlatitude ionosphere or plasmasphere is included.

The simulations presented here run in nearly real time on 49 cores of the National Center for Atmospheric Research (NCAR) Yellowstone supercomputer. The IPWM has been inserted into the model coupling framework developed by the Center for Integrated Space Weather Modeling (CISM). The models run asynchronously using 32 cores for MFLFM, 16 for IPWM, and 1 for MIX. At each exchange time the models exchange data via the InterComm library (www.cs.umd.edu/projects/hpsl/chaos/ResearchAreas/ic/). The scalability of the entire coupled model is limited by the scalability of the MFLFM, which is the most computationally intensive part. The computational expense of the MFLFM scales quartically with the number of cells. When the IPWM horizontal resolution is increased without changing the vertical resolution it scales quadratically with the horizontal resolution since the time step is set by the vertical grid. MIX in a serial elliptic solver that does not scale, but it is a small fraction of the total computational time. In the future we plan to test quadruple-resolution MFLFM on 256 cores coupled to 1° IPWM on 32 cores and 1° MIX on 1 core. We expect that configuration to run at approximately half of real time (i.e., 1 h of simulation time per 2 h of wall clock time).

3. Phenomenological Wave-Particle Interactions Model

Numerous studies with using Freja [*Norqvist et al.*, 1998; *Knudsen et al.*, 1998; *Hamrin et al.*, 2002] and FAST [*Lund et al.*, 2000] data have concluded that ICRH by BBELF is the primary transverse ion acceleration mechanism. Motivated by these studies, the phenomenological WPI model in IPWM only includes ICRH by BBELF. The limitations of this assumption are further discussed in section 4.3. Section 3.1 reviews the rigorous theory of ICRH. Section 3.2 describes the simplified approach employed by the IPWM originally introduced by *Varney et al.* [2015], and section 3.3 validates this approach with comparisons to kinetic simulations. Section 3.4 describes methods for causally regulating the BBELF wave amplitudes using Alfvénic Poynting flux from the MHD model needed to complete the specification of the model.

3.1. Theory of Ion Cyclotron Resonance Heating by BBELF

The distribution function $f_i(\mathbf{r}, \mathbf{v}, t)$ of collisionless ions in a wave field will experience phase-space diffusion governed by a Fokker-Planck equation [*Ichimaru*, 2004]:

$$\left[\frac{\partial}{\partial t} + \mathbf{v}\cdot\frac{\partial}{\partial \mathbf{r}} + \left(\frac{q_i}{m_i}\mathbf{E} + \frac{q_i}{m_i}\mathbf{v}\times\mathbf{B} + \mathbf{g}\right)\cdot\frac{\partial}{\partial \mathbf{v}}\right] f_i(\mathbf{r}, \mathbf{v}, t) = \frac{\partial}{\partial \mathbf{v}}\cdot\mathbf{D}\cdot\frac{\partial}{\partial \mathbf{v}} f_i(\mathbf{r}, \mathbf{v}, t)\,. \tag{1}$$

In this equation $\mathbf{r}$ and $\mathbf{v}$ are the position and velocity; q_i and m_i are the ion charge and mass; and $\mathbf{E}$, $\mathbf{B}$, and $\mathbf{g}$ are the background electric, magnetic, and gravitational fields. In the case of ICRH by BBELF, the phase-space diffusion tensor is dominated by its perpendicular portion, i.e., $\mathbf{D} = D_\perp\left(\mathbf{I} - \hat{b}\hat{b}\right)$, where $\hat{b}$ is the unit vector parallel to $\mathbf{B}$. A complete expression for $D_\perp$ depending on the entire wave spectrum and the particle velocities is given by *Bouhram et al.* [2004]. This expression is dominated by the principle resonance with left-hand circularly polarized (LHCP) waves near the ion gyrofrequency, $\Omega_i = q_i B/m_i$. In the long wavelength limit, the contribution from the principle resonance reduces to the velocity-independent expression [*Chang et al.*, 1986; *Retterer et al.*, 1987; *Crew et al.*, 1990]

$$D_\perp = \frac{\eta q_i^2}{4m_i^2}\left\langle |E|^2\right\rangle(\omega = \Omega_i)\,, \tag{2}$$

where $\left\langle |E|^2\right\rangle(\omega = \Omega_i)$ is the power spectral density (PSD) of electric field fluctuations at the ion gyrofrequency, and η is the fraction of the PSD in LHCP. The remainder of this work will assume $\eta = 0.125$ following *Chang et al.* [1986]. The perpendicular diffusion is closely related to the perpendicular heating rate per particle, $\dot{W}_\perp = 2m_i D_\perp$ [*Crew et al.*, 1990].

In macroscopic particle-in-cell (mac-PIC), also known as generalized semikinetic or hybrid PIC, simulations using kinetic ions with fluid electrons the process of phase-space diffusion can be simulated by introducing

stochastic forces. At each time step a random perpendicular velocity, $\Delta v_\perp$, is added to each particle. In order to follow equation (1) on average, these random velocities are sampled from a Gaussian distribution such that $\left\langle \Delta v_\perp^2 \right\rangle = 4D_\perp \Delta t$, where Δt is the time step [*Barghouthi*, 1997; *Barakat and Schunk*, 2001].

In order to simulate the effects of ICRH one needs to know the wave PSD at the gyrofrequency as a function of altitude. BBELF spectra observed by spacecraft are usually given in the form of power laws in frequency, $\left\langle |E|^2 \right\rangle (\omega) = \left\langle |E|^2 \right\rangle (\omega_0) \times (\omega/\omega_0)^{-\alpha}$, with typical exponents of $\alpha = 1.1 \pm 0.6$ [*Bouhram et al.*, 2003]. If the PSD is assumed to be independent of altitude above some minimum altitude, this yields heating rate profiles of the form

$$\dot{W}_\perp(r) = \dot{W}_{0\perp} \left(\frac{B(r)}{B_0} \right)^{-\alpha} \tag{3}$$

$$\approx \dot{W}_{0\perp} \left(\frac{r}{r_0} \right)^{3\alpha}, \tag{4}$$

where r is the geocentric radius and the second approximate form assumes $B(r) \propto r^{-3}$ for dipole field lines near the pole. The heating rates increase with altitude as the gyrofrequency decreases. Monte Carlo simulations using heating rates of this form have been able to reproduce observed ion conics [*Chang et al.*, 1986; *Retterer et al.*, 1987; *Crew et al.*, 1990] and observed altitude distributions of ion velocity and energy in the cleft ion fountain at altitude above 2000 km [*Bouhram et al.*, 2004]. Analysis of Akebono observations of ion conics suggest continuous perpendicular heating up to at least 10,000 km altitude [*Miyake et al.*, 1993]. These studies have used a variety of assumptions for the lowest altitude at which to apply WPI, with no consensus on how low the WPI should go.

Barghouthi [1997] and *Barghouthi et al.* [1998] challenged the assumption of a constant PSD as a function of altitude and instead proposed that the PSD should be a power law in both frequency and radius, $\left\langle |E|^2 \right\rangle (\omega, r) = \left\langle |E|^2 \right\rangle (\omega_0, r_0) \times (\omega/\omega_0)^{-\alpha} (r/r_0)^{\beta}$. With this assumption, the heating rate profile becomes

$$\dot{W}_\perp(r) = \dot{W}_{0\perp} \left(\frac{B(r)}{B_0} \right)^{-\alpha} \left(\frac{r}{r_0} \right)^{\beta} \tag{5}$$

$$\approx \dot{W}_{0\perp} \left(\frac{r}{r_0} \right)^{3\alpha+\beta}. \tag{6}$$

Using four intervals of Dynamics Explorer-1 data from different altitudes, *Barghouthi et al.* [1998] estimated $3\alpha + \beta = 13.3$ for auroral region O^+. This altitude dependence is much steeper than the $3\alpha = 3 \times 1.7 = 5.1$ rate used by *Chang et al.* [1986]. The DE-1 data at different altitudes used by *Barghouthi et al.* [1998] were collected on different dates during different seasons, and thus, they may be conflating altitudinal and seasonal dependences. The generalized polar wind model *Barakat and Schunk* [2001] adopts the very steep altitude profiles from *Barghouthi et al.* [1998] for its WPI. These profiles put very little wave power at low altitudes, and *Barakat et al.* [2003] found that additional low altitude energization regions needed to be added to generalized polar wind model to reproduce the observed cusp and auroral ion outflows. In that study the outflow produced was very sensitive to the placement of the low-altitude energization regions, with lower altitudes generating much more outflow.

Kasahara et al. [2001] presented a comprehensive climatology of the BBELF PSD at 5 Hz as observed by Akebono over 250–10,000 km altitude. This study shows that average values are 0.3 to 0.5 $(\mathrm{mV/m})^2\,\mathrm{Hz}^{-1}$, with the highest values appearing in the cusp and auroral oval. The highest wave powers are observed in the winter hemisphere. This study shows very little altitude dependence of the wave power at a fixed frequency, although the statistical sampling of the lower altitudes is much worse than the high altitudes. Significant wave power was observed at all altitudes down to the 250 km perigee.

Accurate determination of the altitude dependence of the heating rate will require future coordinated, simultaneous, multispacecraft measurements on conjugate field lines. Given how poorly known the altitude dependence is, for the purpose of this study we will adopt a heating rate in the form of equation (3) above some altitude z_{min}, where both α and z_{min} are adjustable parameters.

3.2. Simplified Transport Equations

Kinetic mac-PIC simulations are too computationally expensive to run two-way coupled to a global MHD model. Kinetic simulations can create a variety of distribution functions, but simulations with ICRH tend to produce distributions consisting of a core population and a nonthermal tail [e.g., *Zeng et al.*, 2006]. Similar distributions are often what is inferred from low-altitude observations [e.g., *Ogawa et al.*, 2008]. With this in mind, [*Varney et al.*, 2015] introduced a simplified model for energetic ion transport wherein the O^+ population is split into thermal and nonthermal portions. The nonthermal portion obeys simplified transport equations derived from conservation of mass, momentum, and first adiabatic invariant for a representative mean particle while neglecting parallel pressure, heat flow, and higher-order moments of the distribution function:

$$\frac{\partial}{\partial t} n_j + \nabla \cdot \left[n_j \mathbf{u}_j \right] = \Upsilon n_i \tag{7}$$

$$\begin{aligned} &\frac{\partial}{\partial t} \left(n_j u_{\|j} \right) + \nabla \cdot \left[n_j u_{\|j} \mathbf{u}_j \right] \\ &\quad = n_j \left(\frac{e}{m_j} E_\| + g_\| + \mathbf{u}_j \mathbf{u}_j : \nabla \hat{b} \right) - \frac{p_{\perp j}}{m_j} \nabla_\| \ln B + \Upsilon n_i u_{\|i} \end{aligned} \tag{8}$$

$$\begin{aligned} &\frac{\partial}{\partial t} \epsilon_j + \nabla \cdot \left[\epsilon_j \mathbf{u}_j \right] - \frac{p_{\perp j}}{m_j} \mathbf{u}_\perp \cdot \nabla_\perp \ln B \\ &\quad = n_j u_{\|j} \left(\frac{e}{m_j} E_\| + g_\| + \mathbf{u}_j \mathbf{u}_j : \nabla \hat{b} \right) + \Upsilon \epsilon_i + \frac{1}{m_j} \dot{W}_\perp n_j. \end{aligned} \tag{9}$$

In these equations n_j, $u_{\|j}$, $p_{\perp j}$, and $\epsilon_j = n_j u_{\|j}^2/2 + p_{\perp j}/m_j$ are the number density, parallel velocity, perpendicular pressure, and energy density per unit mass of nonthermal O^+ and n_i, $u_{\|i}$ and $\epsilon_i = n_i u_{\|i}^2/2 + (3/2) p_i/m_i$ are the corresponding quantities for thermal O^+. The vector velocity is $\mathbf{u}_j = u_{\|j} \hat{b} + \mathbf{E} \times \mathbf{B}/B^2$. Physically, equations (7)–(9) describe conservations of mass, parallel momentum, and energy, respectively. The parallel momentum equation includes mirror-force lifting via the term proportional to $\nabla_\| \ln B$, and the energy equation includes transverse heating via $\dot{W}_\perp$. These equations require an ad hoc promotion rate, Υ, which is the rate at which particles are removed from the thermal fluid and added to the nonthermal fluid. The need for this promotion rate is an artifact of the simplifying assumption of a division between thermal and nonthermal portions.

3.3. Comparison to DyFK Mac-PIC Results

While ICRH theory provides a simple way to relate the $\dot{W}_\perp$ to the wave PSD, the promotion rates are more difficult to justify. Given the ad hoc nature of the promotion rate, the only reasonable way to set it is to perform comparisons with kinetic mac-PIC results. *Zeng and Horwitz* [2007] conducted a series of mac-PIC simulations with the Dynamic Fluid-Kinetic (DyFK) model and reduced the resulting outflow fluxes to a formula representation. *Horwitz and Zeng* [2009] conducted a more expansive set of DyFK simulations and created formula representations for the outflowing densities, velocities, and temperatures. We perform comparisons to these representations both to validate the simplified transport equations and to determine how to set the promotion rate.

In order to perform an unbiased comparison between IPWM and DyFK, we have created a 1-D version of IPWM that reproduces the conditions of the DyFK simulations of *Horwitz and Zeng* [2009] as closely as possible. The 1-D IPWM domain is extended up to 3 R_E altitude. The field line simulated has its footpoint at (77.58°S, 290.19°E) in geographic coordinates and (66.56°S, 0.59°E) in geomagnetic coordinates. The empirical EUV and thermosphere models use conditions for 20 August 1998 with the solar radio flux index $F_{10.7} = 142$, its 81 day average of $F_{10.7A} = 133$, and a geomagnetic index of $A_p = 17$. The BBELF wave amplitude is assumed to be

$$\left\langle |E|^2 \right\rangle = D_{\text{wave}} \left(\frac{6.5\ \text{Hz}}{\Omega_i/2\pi} \right)^{1.7} \tag{10}$$

in the altitude range between 1600 km and 2 R_E, and zero outside of it. In the notation of *Zeng and Horwitz* [2007] and *Horwitz and Zeng* [2009], D_{wave} is the electric field PSD at 6.5 Hz, which for the simulated field line is the O^+ gyrofrequency at approximately 1 R_E altitude. Normally, IPWM uses zero derivative as the upper boundary condition on electron temperature. For the 1-D version for comparison to DyFK, however, we have switched to the condition of $T_e = 8000$ K at 3 R_E used by DyFK [*Wu et al.*, 1999].

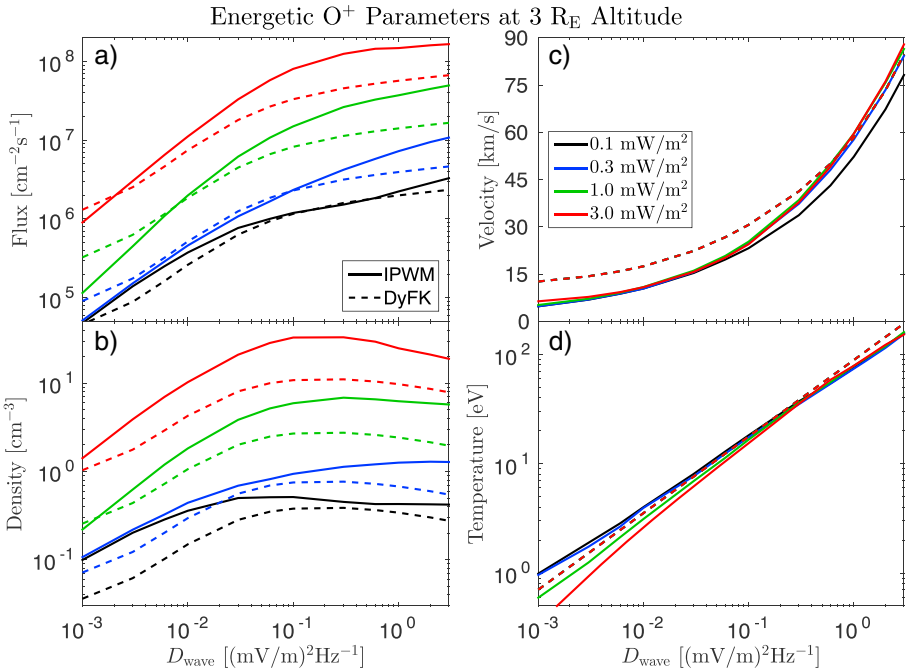

Figure 2. Energetic O^+ parameters at 3 R_E altitude from the tuned, single field line IPWM (solid) and the *Horwitz and Zeng* [2009] formula representations of DyFK results (dashed) as functions of the BBELF electric field power spectral density at 6.5 Hz, D_{wave}. The different colors correspond to different precipitating energy fluxes mapped to 800 km indicated in the legend. The panels show (a) number flux, (b) number density, (c) parallel velocity, and (d) temperature.

Like the DyFK simulations, each simulation begins from a steady polar wind solution derived from a long simulations with no precipitation or wave heating. The precipitation and wave heating are then applied for 2 h. The formulas from *Horwitz and Zeng* [2009] are parameterized in terms of precipitating energy flux, precipitating characteristic energy, solar zenith angle, and D_{wave}. Figure 2 compares the nonthermal O^+ parameters from IPWM to the *Horwitz and Zeng* [2009] formulas for a range of D_{wave} and precipitating energy fluxes. In these comparisons the solar zenith angle is fixed at 114° (i.e., nighttime conditions), and the characteristic energy of the soft precipitation is fixed at 100 eV. The definition of the temperature of the nonthermal O^+ from IPWM used both for this comparison and for passing to MFLFM is the total energy minus the bulk kinetic energy, $T = m_j\epsilon_j - \frac{1}{2}m_j n_j u_{\|j}^2$. These temperatures are compared to the effective isotropic temperatures from DyFK, $T = \frac{1}{3}T_{\|} + \frac{2}{3}T_{\perp}$.

Comparisons of this sort were conducted for a variety of choices for the promotion rate. The results plotted in Figure 2 use an altitude-dependent promotion rate determined by

$$\Upsilon = 5 \times 10^{-3}\dot{W}_{\perp}, \tag{11}$$

where Υ is in s^{-1} and $\dot{W}_{\perp}$ is in eV^{-1}. This relationship was chosen after extensive trial and error with a variety of functional forms, and it consistently produces IPWM fluxes that are within a factor of 3 of the DyFK results. With this relationship, both Υ and $\dot{W}_{\perp}$ scale linearly with D_{wave}. The resultant IPWM fluxes scale nonlinearly with D_{wave}, however. Both DyFK and IPWM predict the outflow flux will increase monotonically with D_{wave}, but will do so at a slower rate above $D_{wave} \approx 10^{-1}(mV/m)^2Hz^{-1}$. A local maximum in the densities appears around this point. *Horwitz and Zeng* [2009] explained this behavior in terms of flux limiting from below. The outflow flux also significantly increases with increasing soft precipitating energy flux since the precipitation modulates electron heating and the resultant type II ion upflow. These simulations do not include any frictional heating or type I ion upflow, but prior experience with the IPWM shows that it has a similar effect [*Varney et al.*, 2015].

The *Horwitz and Zeng* [2009] relationships for the parallel velocity and temperature only depend on D_{wave} since these quantities are insensitive to other parameters in DyFK. IPWM exhibits a similar insensitivity. These quantities are also insensitive to the choice of the promotion rate. The velocity and temperature are per-particle quantities, and thus, they are almost entirely determined by the heating rate per particle, $\dot{W}_{\perp}$. The consistently

good agreement between the IPWM and DyFK velocities and temperatures regardless of the choice of promotion rate validates the simplified transport equations used in IPWM. These equations cannot predict the temperature anisotropy or other higher-order moments of the distribution function, but a global MHD model cannot ingest this information anyway.

3.4. Regulation of BBELF Amplitudes by Alfvénic Poynting Flux

Equations (3) and (11) constrain the free parameters in the WPI model as functions of altitude along a field line to the BBELF wave PSD, but BBELF waves are subgrid scale in the global MHD model. The last element needed to complete the WPI model is to relate BBELF PSD to a parameter the global MHD model can provide. Like *Brambles et al.* [2011], we will use the band-pass-filtered Alfvénic Poynting flux in the 5–180 s period band as a causal regulator of the outflow. The statistical distribution of Alfvénic Poynting flux is similar to that of ion outflows *Chaston et al.* [2007]. The model will assume

$$\left\langle |E|^2 \right\rangle (6.5\,\mathrm{Hz}) = \gamma S_{\parallel}, \tag{12}$$

where $S_{\parallel}$ is the Alfvénic Poynting flux mapped to 100 km and γ is an adjustable parameter. *Kasahara et al.* [2001] show that typical wave PSD are 0.5 $(\mathrm{mV/m})^2\mathrm{Hz}^{-1}$. Experience with the LFM model shows that typical Alfvénic Poynting fluxes are in the range of 10^{-2} to 10^{-1} $\mathrm{mW/m^2}$ [*Zhang et al.*, 2012, 2014]. A reasonable order-of-magnitude estimate of the range of γ is between 5 and 50 $(\mathrm{mV/m})^2\mathrm{Hz}^{-1}/(\mathrm{mW/m^2})$. The sequence of equation (3), (11), and (12) completely specifies the altitude-dependent heating and promotion rates as linear functions of the Alfvénic Poynting flux.

4. Example Simulations

The coupled model has a number of free parameters whose values are poorly constrained. These include the minimum altitude at which to apply WPI (z_{min}), the BBELF spectral index (α) which determines the altitude dependence of the WPI, and the scale factor between the Alfvénic Poynting flux and the BBELF amplitudes (γ). After extensive experimentation with a variety of parameters, we have chosen six illustrative simulations to present that cover a variety of different behaviors observed in the coupled simulations. Comparing and contrasting these simulations gives an appreciation for how outflow can affect the coupled system dynamics and the specific effects that are attributable to various properties of the outflow.

4.1. Simulation Configurations

The six illustrative simulations will henceforth be named runs A–F and are summarized in Table 1. Run A is a baseline single-fluid LFM run that only includes the solar wind H^+ fluid. The hard wall boundary conditions in LFM ensure this run has no ionospheric mass input whatsoever. Run B is a baseline classical polar wind run with no WPI. In this run, the MFLFM uses three fluids: solar wind H^+, thermal polar wind H^+, and thermal polar wind O^+. For runs C–F, MFLFM uses four fluids: solar wind H^+, thermal polar wind H^+, thermal polar wind O^+, and energetic O^+. Run C uses $\gamma = 100\,(\mathrm{mV/m})^2\mathrm{Hz}^{-1}/(\mathrm{mW/m^2})$, $z_{\mathrm{min}} = 600$ km, and $\alpha = 0.6$, which is an aggressive set of WPI parameters designed to produce copious energetic O^+ outflow. This γ implies BBELF wave amplitudes roughly an order of magnitude larger than typical Akebono observations. These choices cause the distribution of WPI with altitude to emphasize acceleration at low altitudes where the thermal plasma density is highest. In general, putting more WPI at lower altitudes produces more outflow.

The parameters for run C should be regarded as upper limits for the values of the free parameters, and this run produces abundant outflow from all locations. Runs D–F were designed to preferentially emphasize the nightside auroral oval, where the Alfvénic Poynting fluxes are most intense. Run F uses the same WPI parameters as C, but WPI is only applied when $S_{\parallel} > 0.1\mathrm{mW/m^2}$. Runs D and E represent a middle ground between runs C and F. Runs D and E use the same γ (PSD per unit input Alfvénic power) and α (PSD power law exponent) as run C, but the transverse ion acceleration starts at higher altitude for lower values of the Alfvénic Poynting flux $S_{\parallel}$, thereby smoothly decreasing the outflow at lower levels of $S_{\parallel}$. The mathematical expressions used are given in Table 1. When the lower altitude of WPI is above the 8400 km upper boundary of the IPWM, WPI is disabled. The model formulations for z_{min} for runs D and E both approach 600 km when $S_{\parallel} \gg 0.1\mathrm{mW/m^2}$ and ∞ when $S_{\parallel} \ll 0.1\mathrm{mW/m^2}$. The transition between these two limits is sharper in run E than in run D, meaning run E is more similar to run F. Signatures of transverse ion acceleration have been observed as low as 600 km [e.g., *Ogawa et al.*, 2008], but acceleration at these low altitudes is not common. Runs D-F are more realistic than run C in that they only apply low-altitude heating when the Alfvénic Poynting flux is largest.

Table 1. Summary of the Configuration and Results of the Example Simulations[a]

Example Simulations				
Run	# of Species	WPI Min Altitude (km)	Mean Hemispheric O^+ Outflow	Convection Mode
A	1	NA	0.00	SMC
B	3	None	0.49×10^{26} ions/s	SMC
C	4	600	1.66×10^{26} ions/s	SMC
D	4	$600 + 400\left(\frac{S}{0.1}\right)^{-2/3}$	1.30×10^{26} ions/s	Sawteeth
E	4	$600 + 50\left(\frac{S}{0.1}\right)^{-2}$	1.79×10^{26} ions/s	Sawteeth
F	4	600 iff $S \geq 0.1$	1.66×10^{26} ions/s	Sawteeth

[a]NA: not applicable.

All six runs use identical initial conditions and identical SW/IMF conditions. All the simulations use steady solar wind with a number density of 5cm^{-3}, an SM X velocity of -400km/s, no SM Y, or SM Z velocity, and a sound speed of 40km/s (≈10eV). The SM X and SM Y components of the IMF are always zero, and only the B_z component changes in time. The initial condition for the MFLFM was constructed using a standard technique for initializing the single-fluid LFM. The single-fluid LFM-MIX is run for 2 h with $B_z = -5$nT followed by another 2 h with $B_z = +5$nT. The IPWM is initialized by running for 12 h using constant MIX inputs from the end of the IMF northward period. The solar conditions are nominally for 21 March 2002 and $F_{10.7} = 200$ solar flux units, i.e., equinox and solar maximum.

In each of the six runs the model coupling begins at simulation time 04:00. The IMF B_z remains at +5nT from 04:00 to 05:00, then linearly transitions from +5 to −10nT over 05:00 to 06:00, crossing through zero at 05:20. It then remains at −10nT for another 10 or 14 h as described in section (4.2). By initiating the model coupling before the southward turning, the classical polar wind has sufficient time to populate the MFLFM domain before the main event begins. The steady SW/IMF conditions from 06:00 onward are identical to runs A–F of *Brambles et al.* [2011].

4.2. Results

Figure 3 summarizes the results of the six runs. The panels show the MIX cross polar cap potential (CPCP), the polar cap open flux determined by tracing field lines in the MFLFM, the hemispherically integrated IPWM O^+ outflow rate summed over both O^+ species, and the hemispherically integrated Alfvénic power. Table 1 quotes the hemispheric outflow rates averaged from 08:00 onward. Runs A and B stop at 16:00, but they have clearly reached a steady state by this time. These hemispheric values should be doubled to compare to the total outflow rate values quoted by *Brambles et al.* [2011].

Counterintuitively, runs C through F have similar average outflow rates even though runs D through F are applying the WPI less frequently than run C. A difficulty with tuning the WPI model is that the distribution of Alfvénic Poynting flux is itself a function of the outflow. Run C produces by far the least integrated Alfvénic power of all the simulations, with the most being produced by runs A and F. The mechanisms by which the outflow in run C suppresses the generation of Alfvénic Poynting flux requires further investigation.

The CPCP in runs C through F are decreased approximately 40 kV relative to runs A and B in agreement with the well-known result that the presence of heavy ions in the magnetosphere decreases the CPCP [*Winglee et al.*, 2002; *Brambles et al.*, 2010; *Welling and Zaharia*, 2012]. Our companion paper shows that the dayside reconnection potentials in runs C through F are also reduced relative to those in run A, in agreement with the prediction that dayside mass loading should reduce the reconnection potential [*Zhang et al.*, 2016b]. Even though the CPCP from run B is comparable to run A, the open flux toward the end of the simulation in run B is much larger than in run A. This distinction indicates that even without WPI, the classical polar wind is having some effect on the magnetospheric configuration.

All six runs exhibit an initial substorm at 06:15 to 06:30 triggered by the initial southward turning, but the effect of this substorm on the net open flux varies considerably between the runs. The rate of reduction of the net open flux depends on the difference between the dayside and nightside reconnection rates. Run A contains no heavy ions, and run B contains relatively few heavy ions during the early part of the simulation. The initial substorms in both of these runs produce large nightside reconnection rates and significant reductions

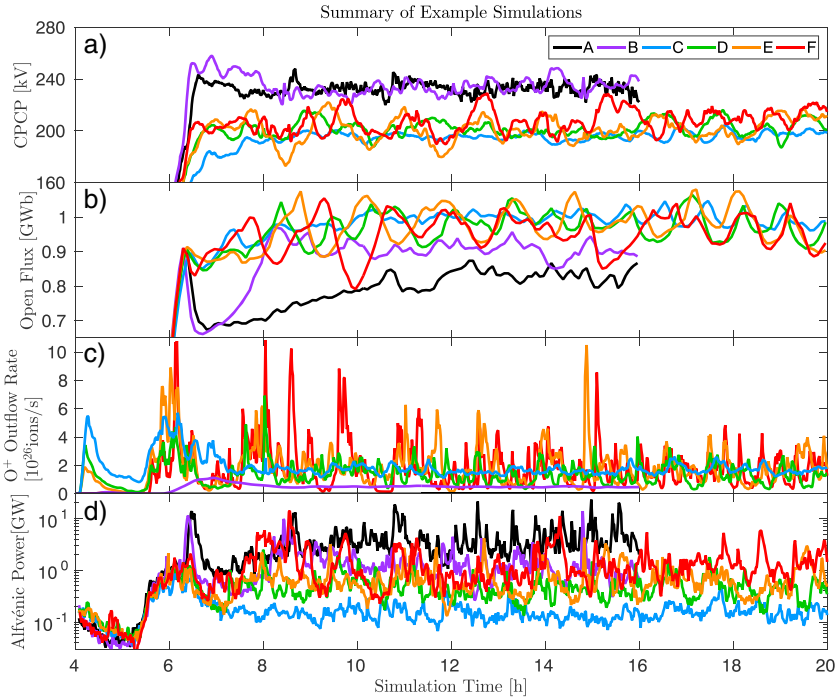

Figure 3. Summary of the example simulations. The panels show (a) the cross polar cap potential, (b) the polar cap open flux, (c) the hemispheric O^+ outflow rate, and (d) the integrated Alfvénic power. Sawtooth oscillations appear as ~2 h oscillations in the CPCP and open flux.

in the open flux between 06:15 and 07:00. In runs C through F, however, the tail contains significant densities of heavy ions at the time of the initial substorm that reduce the nightside reconnection rates. In these simulations the nightside reconnection rates during the first substorm barely exceed the dayside reconnection rates, resulting in only a modest net decrease in the open flux following the initial substorm. Our companion paper presents more analysis of the reconnection rates in these simulations.

Runs D–F exhibit oscillations in the CPCP with ~2 h periods. These oscillations are also apparent in the open flux, and the increases in CPCP correspond with abrupt decreases in the open flux. These events also correspond to bursts in the Alfvénic power and the ion outflow. In our companion paper we assert that these bursts are sawtooth oscillations and provide detailed analysis of their mechanism of generation.

4.3. Plausibility of Outflow

Given the assumptions made in constructing the illustrative simulations, it is reasonable to question if any of them produce plausible outflow distributions. If the statistical properties of the outflow as a function of the Alfvénic Poynting flux agree with observations, then the outflow is at least plausible.

The study of *Brambles et al.* [2011] uses an empirical relationship between Alfvénic Poynting flux and O^+ outflow flux that was determined from FAST satellite data at 4000 km altitude. Studying the IPWM state at 4000 km allows a direct comparison to that relationship. Figure 4 shows the 15 min averaged energetic O^+ flux at 4000 km in the IPWM as a function of the 15 min averaged Alfvénic Poynting flux for every modeled flux tube. Also shown are power law fits to all the points above $10^6 cm^{-2}s^{-1}$. The 15 min time period is comparable to the typical time delay between the application of wave heating and the appearance of outflows at 4000 km [*Varney et al.*, 2015]. The fluxes in run C are almost always above the empirical relationship, and yet the slope with increasing Poynting flux is too shallow. Runs D–F were designed to make this slope steeper, and runs D and E are in fairly good agreement with the empirical relationship. The simulation results have a lot of scatter around the power law relationship, as does the FAST data from which that relationship was derived. Even though the WPI in the model is a deterministic function of the Alfvénic Poynting flux, the outflow flux it produces depends on the supply of thermal plasma to the heating regions and the residence time in the heating regions as the plasma convects.

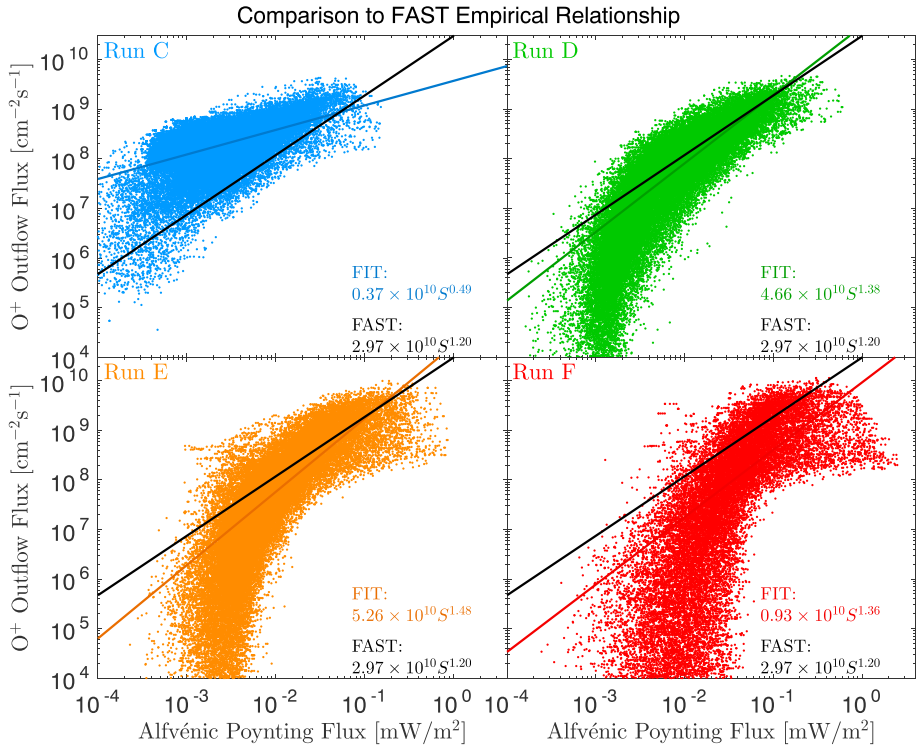

Figure 4. Fifteen minute averaged energetic O^+ outflow flux at 4000 km altitude inside IPWM as a function of 15 min averaged Alfvénic Poynting flux for runs C–F. The colored lines are power law fits, and the black lines are the empirical relationship derived from FAST data at 4000 km used by *Brambles et al.* [2011].

The scatter plots in Figure 4 also exhibit an upper limit on the outflow flux that is not captured by a simple power law relationship. The model fluxes never exceed 10^{10}cm^{-2}s^{-1} no matter how intense the Alfvénic Poynting flux becomes. The reasons for this behavior in the model are twofold. First, none of the relationships for z_{min} ever go below 600 km no matter how intense $S_{||}$ becomes. The second reason is the flux-limiting behavior illustrated in Figure 2.

Runs C through F use a high value for γ that produces wave PSD for WPI that are larger than typical observations. Despite these high values, runs D and E are producing good agreement with the FAST empirical relationship. This finding may imply that ICRH alone does not completely explain the ion acceleration, and the large wave PSD are compensating for other acceleration effects missing in IPWM. Expanding IPWM to include a better specification of the full wave spectrum and all the relevant WPI mechanisms will require much more information from observations than is currently available.

5. Discussion and Conclusions

The coupled model described in this work provides a powerful tool for investigating the influence of heavy ion outflow on geospace system dynamics. In order to produce an outflow model that is practical to run alongside a global MHD model, the IPWM makes numerous simplifications of the true kinetic physics of the polar wind. Nonetheless, comparisons with the DyFK formula representations from *Horwitz and Zeng* [2009] shows surprisingly good agreement between the simplified model and the kinetic model. More intermodel comparisons between this model and other kinetic models are needed, however, to fully understand the impacts of the missing physics.

The IPWM is more realistic than an empirical model in many important aspects including conservation of mass between the ionosphere and magnetosphere and realistic limitation of the ion outflow flux by the limited ion upflow from below. The outflows introduced have significant effects on the dynamics of the coupled system and can drive behaviors not seen in single-fluid MHD simulations, such as internally driven sawtooth oscillations.

The simulation results demonstrate the close connection between the underlying physics regulating ionospheric outflow and its impacts on the coupled system dynamics. Key parameters of the physics-based model presented here are not well constrained by either theory or observations, and further exploration of the parameter space under a wider variety of SW/IMF conditions is needed. A subset of the parameter space examined here produces reasonable agreement with the FAST empirical relationship. The altitude dependence of the energization in particular has a dramatic effect on the distribution of outflow. This altitude dependence is impossible to determine from single satellite measurements and remains poorly understood.

The major strength of the coupled model is its physical framework for investigating a variety of different simulations with different kinds of outflow. Comparing and contrasting such ensembles of runs provides insight into how the outflow influences the coupled dynamics and which aspects of the ion outflow are responsible for various observed effects. Our companion paper analyzes the same six example simulations presented here in more detail in order to determine how and why some of the simulations develop sawtooth oscillations while others do not. In the future, we intend use this model to conduct more comparative studies of this sort for both idealized and real events in order to gain a deeper understanding of how outflow affects the geospace system.

Acknowledgments
This work is supported by National Science Foundation grant AGS-1555801. The National Center for Atmospheric Research is sponsored by the National Science Foundation. We would like to acknowledge high-performance computing support from Yellowstone (ark:/85065/d7wd3xhc) provided by NCAR's Computational and Information Systems Laboratory, sponsored by the National Science Foundation. All source code and model output are archived on the NCAR High Performance Storage System and is available upon request.

References

Abe, T., B. A. Whalen, A. W. Yau, R. E. Horita, S. Watanabe, and E. Sagawa (1993a), EXOS D (Akebono) suprathermal mass spectrometer observations of the polar wind, *J. Geophys. Res.*, *98*(A7), 11,191–11,203.

André, M., and A. Yau (1997), Theories and observations of ion energization and outflow in the high latitude magnetosphere, *Space Sci. Rev.*, *80*, 27–48.

Axford, W. I. (1968), The polar wind and the terrestrial helium budget, *J. Geophys. Res.*, *73*, 6855–6859.

Banks, P. M., and T. E. Holzer (1969), Features of plasma transport in the upper atmosphere, *J. Geophys. Res.*, *74*, 6304–6316.

Barakat, A. R., and R. W. Schunk (2001), Effects of wave-particle interactions on the dynamic behavior of the generalized polar wind, *J. Atmos. Solar-Terr. Phys.*, *63*, 75.

Barakat, A. R., R. W. Schunk, and H. G. Demars (2003), Seasonal and solar activity dependence of the generalized polar wind with low-altitude auroral ion energization, *J. Geophys. Res.*, *108*(A11), 1405, doi:10.1029/2002JA009360.

Barghouthi, I. A. (1997), Effects of wave-particle interactions on H^+ and O^+ outflow at high latitude: A comparative study, *J. Geophys. Res.*, *102*(A10), 22,065–22,075.

Barghouthi, I. A., A. R. Barakat, and A. M. Persoon (1998), The effects of altitude-dependent wave particle interactions in the polar wind plasma, *Astrophys. Space Sci.*, *259*, 117–140.

Bennett, E. L., M. Temerin, and F. S. Mozer (1983), The distribution of auroral electrostatic shocks below 8000 km altitude, *J. Geophys. Res.*, *88*(A9), 7107–7120, doi:10.1029/JA088iA08p07107.

Bouhram, M., M. Malingre, J. R. Jasperse, N. Nubouloz, and J.-A. Sauvaud (2003), Modeling transverse heating and outflow of ionospheric ions from the dayside cusp/cleft. 2. Applications, *Ann. Geophys.*, *21*, 1773–1791.

Bouhram, M., B. Klecker, W. Miyake, H. Rème, J.-A. Sauvaud, M. Malingre, L. Kistler, and A. Blågàu (2004), On the altitude dependence of transversely heated O^+ distributions in the cusp/cleft, *Ann. Geophys.*, *22*, 1787–1798.

Brambles, O. J., W. Lotko, P. A. Damiano, B. Zhang, M. Wiltberger, and J. Lyon (2010), Effects of causally driven cusp O^+ outflow on the storm time magnetosphere-ionosphere system using a multifluid global simulation, *J. Geophys. Res.*, *115*, A00J04, doi:10.1029/2010JA015469.

Brambles, O. J., W. Lotko, B. Zhang, M. Wiltberger, J. Lyon, and R. J. Strangeway (2011), Magnetosphere sawtooth oscillations induced by ionospheric outflow, *Science*, *332*(6034), 1183–1186, doi:10.1126/science.1202869.

Brambles, O. J., W. Lotko, B. Zhang, J. Ouellette, J. Lyon, and M. Wiltberger (2013), The effects of ionospheric outflow on CME and SIR driven sawtooth events, *J. Geophys. Res. Space Physics*, *118*, 6026–6041, doi:10.1002/jgra.50522.

Chang, T., and B. Coppi (1981), Lower hybrid acceleration and ion evolution in the suprauroral region, *Geophys. Res. Lett.*, *8*, 1253–1256.

Chang, T., G. B. Crew, H. Hershkowitz, J. R. Jasperse, and J. M. Retterer (1986), Transverse acceleration of oxygen ions by eletromagnetic in cyclotron resonance with broadband left-hand-polarized waves, *Geophys. Res. Lett.*, *13*, 636–639.

Chaston, C. C., J. W. Bonnell, C. W. Carlson, J. P. McFadden, R. E. Ergun, R. J. Strangeway, and E. J. Lund (2004), Auroral ion acceleration in dispersive Alfvén waves, *J. Geophys. Res.*, *109*, A04205, doi:10.1029/2003JA010053.

Chaston, C. C., C. W. Carlson, J. P. McFadden, R. E. Ergun, and R. J. Strangeway (2007), How important are dispersive Alfvén waves for auroral particle acceleration?, *Geophys. Res. Lett.*, *34*, L07101, doi:10.1029/2006GL029144.

Cladis, J. B. (1986), Parallel acceleration and transport of ions from polar ionosphere to plasma sheet, *Geophys. Res. Lett.*, *13*(9), 893–896.

Cohen, I. J., M. R. Lessard, R. H. Varney, K. Oksavik, M. Zettergren, and K. A. Lynch (2015), Ion upflow dependence on ionospheric density and solar photoionization, *J. Geophys. Res. Space Physics*, *120*, 10,039–10,052, doi:10.1002/2015JA021523.

Coley, W. R., R. A. Heelis, and M. R. Hairston (2003), High-latitude plasma outflow as measured by the DMSP spacecraft, *J. Geophys. Res.*, *108*(A12), 1441, doi:10.1029/2003JA009890.

Crew, G. B., T. Chang, J. M. Retterer, W. K. Peterson, D. A. Gurnett, and R. L. Huff (1990), Ion cyclotron resonance heated conics: Theory and observations, *J. Geophys. Res.*, *95*(A4), 3959–3985.

Ebihara, Y., M. Yamada, S. Watanabe, and M. Ejiri (2006), Fate of outflowing suprathermal oxygen ions that originate in the polar ionosphere, *J. Geophys. Res.*, *111*, A04219, doi:10.1029/2005JA011403.

Fang, X., C. E. Randall, D. Lummerzheim, S. C. Solomon, M. J. Mills, D. R. Marsh, C. H. Jackman, W. Wang, and G. Lu (2008), Electron impact ionization: A new parameterization for 100 eV to 1 MeV electrons, *J. Geophys. Res.*, *113*, A09311, doi:10.1029/2008JA013384.

Fedder, J. A., S. P. Slinker, J. G. Lyon, and R. D. Elphinstone (1995), Global numerical simulation of the growth phase and expansion onset for a substorm observed by Viking, *J. Geophys. Res.*, *100*, 19,083–19,093.

Fridman, M., and J. Lemaire (1980), Relationship between auroral electron fluxes and field aligned electric potential difference, *J. Geophys. Res.*, *85*, A2664, doi:10.1029/JA085iA02p00664.

García, K. S., V. G. Merkin, and W. J. Hughes (2010), Effects of nightside O^+ outflow on magnetospheric dynamics: Results of multifluid MHD modeling, *J. Geophys. Res.*, *115*, A00J09, doi:10.1029/2010JA015730.

Garcia-Sage, K., T. E. Moore, A. Pembroke, V. G. Merkin, and W. J. Hughes (2015), Modeling the effects of ionospheric oxygen outflow on bursty magnetotail flows, *J. Geophys. Res. Space Physics*, *120*, 8723–8737, doi:10.1002/2015JA021228.

Glocer, A. (2015), *The Role of Superthermal Electrons in High Latitude Ionospheric Outflows*, Inner Magnetospheric Coupling-III Workshop, Los Angeles, Calif.

Glocer, A., G. Tóth, T. Gombosi, and D. Welling (2009a), Modeling ionospheric outflows and their impact on the magnetosphere, initial results, *J. Geophys. Res.*, *114*, A05216, doi:10.1029/2009JA014053.

Glocer, A., G. Tóth, Y. J. Ma, T. Gombosi, J.-C. Zhang, and L. M. Kistler (2009b), Multifluid Block-Adaptive-Tree Solar wind Roe-type Upwind Scheme: Magnetospheric composition and dynamics during geomagnetic storms-Initial results, *J. Geophys. Res.*, *114*, A12203, doi:10.1029/2009JA014418.

Glocer, A., N. Kitamura, G. Toth, and T. Gombosi (2012), Modeling solar zenith angle effects on the polar wind, *J. Geophys. Res.*, *117*, A04318, doi:10.1029/2011JA017136.

Guglielmi, A., and R. Lundin (2001), Ponderomotive upward acceleration of ions by ion cyclotron and Alfvén waves over the polar regions, *J. Geophys. Res.*, *106*(A7), 13,219–13,236, doi:10.1029/2000JA900066.

Hamrin, M., P. Norqvist, T. Hellström, M. André, and A. I. Eriksson (2002), A statistical study of ion energization at 1700 km in the auroral region, *Ann. Geophys.*, *20*(12), 1943–1958.

Horwitz, J. L., and W. Zeng (2009), Physics-based formula representations of high-latitude ionospheric outflows: H^+ and O^+ densities, flow velocities, and temperatures versus soft electron precipitation, wave-driven transverse heating, and solar zenith angle effects, *J. Geophys. Res.*, *114*, A01308, doi:10.1029/2008JA013595.

Ichimaru, S. (2004), *Statistical Plasma Physics*, vol. 1, Westview Press, Boulder, Colo.

Kasahara, Y., T. Hosoda, T. Mukai, S. Watanabe, I. Kimura, H. Kojima, and R. Niitsu (2001), ELF/VLF waves correlated with transversely accelerated ion in the auroral region observed by Akebono, *J. Geophys. Res.*, *106*(A10), 21,123–21,136.

Khazanov, G. V., M. W. Liemohn, and T. E. Moore (1997), Photoelectron effects on the self-consistent potential in the collisionless polar wind, *J. Geophys. Res.*, *102*(A4), 7509–7521.

Khazanov, G. V., M. W. Liemohn, E. N. Krivorutsky, and T. E. Moore (1998), Generalized kinetic description of a plasma in an arbitrary field-aligned potential energy structure, *J. Geophys. Res.*, *103*, 6871–6889.

Kintner, P. M., J. Franz, P. Schuck, and E. Klatt (2000), Interferometric coherency determination of wavelength or what are broadband ELF waves?, *J. Geophys. Res.*, *105*(A9), 21,237–21,250, doi:10.1029/1999JA000323.

Knight, S. (1973), Parallel electric fields, *Planet. Space Sci.*, *21*, 741–750.

Knudsen, D. J., J. H. Clemmons, and J.-E. Wahlund (1998), Correlation between core ion energization, suprathermal electron bursts, and broadband ELF plasma waves, *J. Geophys. Res.*, *103*(A3), 4171–4186.

Kronberg, E. A., et al. (2014), Circulation of heavy ions and their dynamic effects in the magnetosphere: Recent observations and models, *Space Sci. Rev.*, *184*, 173–235, doi:10.1007/s11214-014-0104-0.

Lennartsson, O. W., H. L. Collin, and W. K. Peterson (2004), Solar wind control of Earth's H^+ and O^+ outflow rates in the 15-eV to 33-keV energy range, *J. Geophys. Res.*, *109*, A12212, doi:10.1029/2004JA010690.

Lockwood, M., M. O. Chandler, J. L. Horwitx, J. H. Waite Jr., T. E. Moore, and C. R. Chappell (1985), The cleft ion fountain, *J. Geophys. Res.*, *90*, 9736–9748.

Loranc, M., W. B. Hanson, R. A. Heelis, and J.-P. St. Maurice (1991), A morphological study of vertical ionospheric flows in the high-latitude *F* region, *J. Geophys. Res.*, *96*, 3627–3646.

Lund, E. J., et al. (2000), Transverse ion acceleration mechanisms in the aurora at solar minimum: Occurrence distributions, *J. Atmos. Sol. Terr. Phys.*, *62*, 467–475.

Lyon, J. G., J. A. Fedder, and C. M. Mobarry (2004), The Lyon-Fedder-Mobarry (LFM) global MHD magnetospheric simulation code, *J. Atmos. Sol. Terr. Phys.*, *66*, 1333–1350, doi:10.1016/j.jastp.2004.02.020.

Merkin, V. G., and J. G. Lyon (2010), Effects of the low-altitude ionospheric boundary condition on the global magnetosphere, *J. Geophys. Res.*, *115*, A10202, doi:10.1029/2010JA015461.

Miyake, W., T. Mukai, and N. Kaya (1993), On the evolution of ion conics along the field line from EXOS D observations, *J. Geophys. Res.*, *98*(A7), 11,127–11,134, doi:10.1029/92JA00716.

Moore, T. E., and G. V. Khazanov (2010), Mechanisms of ionospheric mass escape, *J. Geophys. Res.*, *115*, A00J13, doi:10.1029/2009JA014905.

Norqvist, P., M. André, and M. Tyrland (1998), A statistical study of ion energization mechanisms in the auroral region, *J. Geophys. Res.*, *103*(A10), 23,459–23,473.

Ogawa, Y., et al. (2008), Coordinated EISCAT Svalbard radar and Reimei satellite observations of ion upflows and suprathermal ions, *J. Geophys. Res.*, *113*, A05306, doi:10.1029/2007JA012791.

Ouellette, J. E., O. J. Brambles, J. G. Lyon, W. Lotko, and B. N. Rogers (2013), Properties of outflow-driven sawtooth substorms, *J. Geophys. Res. Space Physics*, *118*, 3223–3232, doi:10.1002/jgra.50309.

Peterson, W. K., L. Andersson, B. C. Callahan, H. L. Collin, J. D. Scudder, and A. W. Yau (2008), Solar-minimum quiet time ion energization and outflow in dynamic boundary-related coordinates, *J. Geophys. Res.*, *113*, A07222, doi:10.1029/2008JA013059.

Picone, J. M., A. E. Hedin, D. P. Drob, and A. C. Aikin (2002), NRLMSISE-00 empirical model of the atmosphere: Statistical comparisons and scientific issues, *J. Geophys. Res.*, *107*, 1468, doi:10.1029/2002JA009430.

Redmon, R. J., W. K. Peterson, L. Andersson, E. A. Kihn, W. F. Denig, M. Hairston, and R. Coley (2010), Vertical thermal O^+ flows at 850 km in dynamic auroral boundary coordinates, *J. Geophys. Res.*, *115*, A00J08, doi:10.1029/2010JA015589.

Retterer, J. M., T. Chang, G. B. Crew, J. R. Jasperse, and J. D. Winningham (1987), Monte Carlo modeling of ionospheric oxygen acceleration by cyclotron resonance with broad-band electromagnetic turbulence, *Phys. Rev. Lett.*, *59*, 148–151.

Richards, P. G., T. N. Woods, and W. K. Peterson (2006), HEUVAC: A new high resolution solar EUV proxy model, *Adv. Space Res.*, *37*, 315–322.

Robinson, R. M., R. R. Vondrak, K. Miller, T. Babbs, and D. A. Hardy (1987), On calculating ionospheric conductivities from the flux and energy of precipitating electrons, *J. Geophys. Res.*, *92*(A3), 2565–2569.

Sharp, R. D., R. G. Johnson, and E. G. Shelley (1977), Observation of an ionospheric acceleration mechanism producing energetic (keV) ions primarily normal to the geomagnetic field direction, *J. Geophys. Res.*, *82*, 3324–3328.

Shay, M. A., and M. Swisdak (2004), Three-species collisionless reconnection: Effect of O^+ on magnetotail reconnection, *Phys. Rev. Lett.*, *93*(17), 175001, doi:10.1103/PhysRevLett.93.175001.

Shelley, E., R. Johnson, and R. Sharp (1972), Satellite observations of energetic heavy ions during a geomagnetic storm, *J. Geophys. Res.*, *77*(31), 6104–6110.

Shelley, E. G., R. D. Sharp, and R. G. Johnson (1976), Satellite observations of an ionospheric acceleration mechanism, *Geophys. Res. Lett.*, *3*, 654–656.

Strangeway, R. J., R. E. Ergun, Y.-J. Su, C. W. Carlson, and R. C. Elphic (2005), Factors controlling ionospheric outflows as observed at intermediate altitudes, *J. Geophys. Res.*, *110*, A03221, doi:10.1029/2004JA010829.

Temerin, M., and I. Roth (1986), Ion heating by waves with frequencies below the ion gyrofrequency, *Geophys. Res. Lett.*, *13*(11), 1109–1112.

Varney, R. H., S. C. Solomon, and M. J. Nicolls (2014), Heating of the sunlit polar cap ionosphere by reflected photoelectrons, *J. Geophys. Res. Space Physics*, *119*, 1–25, doi:10.1002/2013JA019378.

Varney, R. H., M. Wiltberger, and W. Lotko (2015), Modeling the interaction between convection and nonthermal ion outflows, *J. Geophys. Res. Space Physics*, *120*, 2353–2362, doi:10.1002/2014JA020769.

Wahlund, J.-E., H. J. Opgenoorth, I. H. K. J. Winser, and G. O. L. Jones (1992), EISCAT observations of topside ionospheric ion outflows during auroral activity: Revisited, *J. Geophys. Res.*, *97*, A33019.

Welling, D. T., and M. W. Liemohn (2014), Outflow in global magnetohydrodynamics as a function of a passive inner boundary source, *J. Geophys. Res. Space Physics*, *119*, 2691–2705, doi:10.1002/2013JA019374.

Welling, D. T., and S. G. Zaharia (2012), Ionospheric outflow and cross polar cap potential: What is the role of magnetospheric inflation?, *Geophys. Res. Lett.*, *39*(2), L23101, doi:10.1029/2012GL05228.

Welling, D. T., V. K. Jordanova, A. Glocer, G. Toth, M. W. Liemohn, and D. R. Weimer (2015), The two-way relationship between ionospheric outflow and the ring current, *J. Geophys. Res. Space Physics*, *120*, 4338–4353, doi:10.1002/2015JA021231.

Wiltberger, M. (2015), Review of global simulation studies of the effect of ionospheric outflow on the magnetosphere-ionosphere system dynamics, in *Magnetotails in the Solar System*, edited by A. Keiling, C. M. Jackman, and P. A. Delamere, John Wiley Inc., Hoboken, N. J., doi:10.1002/9781118842324.ch22.

Wiltberger, M., R. S. Weigel, W. Lotko, and J. A. Fedder (2009), Modeling seasonal variations of auroral particle precipitation in a global-scale magnetosphere-ionopshere simulation, *J. Geophys. Res.*, *114*, A01204, doi:10.1029/2008JA013108.

Wiltberger, M., W. Lotko, J. G. Lyon, P. Damiano, and V. Merkin (2010), Influence of cusp O^+ outlfow on magnetotail dynamics in a multifluid MHD model of the magnetosphere, *J. Geophys. Res.*, *115*, A00305, doi:10.1029/2010JA015579.

Winglee, R. M. (1998), Multifluid simulations of the magnetosphere: The identification of the geopause and its variation with IMF, *Geophys. Res. Lett.*, *25*, 4441–4444, doi:10.1029/1998GL900217.

Winglee, R. M., D. Chua, M. Brittnacher, G. K. Parks, and G. Lu (2002), Global impact of ionospheric outflows on the dynamics of magnetosphere and cross-polar cap potential, *J. Geophys. Res.*, *107*(A9), 1237, doi:10.1029/2001JA000214.

Wu, X.-Y., J. L. Horwitz, G. M. Estep, Y.-J. Su, D. G. Brown, P. G. Richards, and G. R. Wilson (1999), Dynamic fluid-kinetic (DyFK) modeling of auroral plasma outflow driven by soft electron precipitation and transverse heating, *J. Geophys. Res.*, *104*(A8), 17,263–17,275.

Yau, A. W., and M. André (1997), Sources of ion outflow in the high latitude ionosphere, *Space Sci. Rev.*, *80*(1), 1–25.

Yau, A. W., E. G. Shelley, W. K. Peterson, and L. Lenchyshyn (1985), Energetic auroral and polar ion outflow at DE-1 altitudes: Magnitude, composition, magnetic activity dependence, and long term variations, *J. Geophys. Res.*, *90*, 8417–8432.

Yau, A. W., W. K. Peterson, and E. G. Shelley (1988), Quantitative parameterization of energetic ionospheric ion outflow, in *Modeling Magnetospheric Plasma*, edited by T. E. Moore et al., American Geophysical Union, Washington, D. C., doi:10.1029/GM044p0211.

Yau, A. W., W. K. Peterson, and T. Abe (2011), Influences of the ionosphere, thermosphere and magnetosphere on ion outflows, in *The Dynamic Magnetosphere*, IAGA Special Sopron Book Series, vol. 3, edited by A. W. Yau, W. K. Peterson, and T. Abe, pp. 283–314, Springer, Netherlands, doi:10.1007/978-94-007-0501-2_16.

Yu, Y., and A. J. Ridley (2013), Exploring the influence of ionospheric O^+ outflow on magnetospheric dynamics: Dependence on the source location, *J. Geophys. Res. Space Physics*, *118*(4), 1711–1722, doi:10.1029/2012JA018411.

Zeng, W., and J. L. Horwitz (2007), Formula representation of auroral ionospheric O^+ outflows based on systematic simulations with effects of soft electron precipitation and transverse ion heating, *Geophys. Res. Lett.*, *34*, L06103, doi:10.1029/2006GL028632.

Zeng, W., J. L. Horwitz, and J.-N. Tu (2006), Characteristic ion distributions in the dynamic auroral transition region, *J. Geophys. Res.*, *111*, A04201, doi:10.1029/2005JA011417.

Zhang, B., W. Lotko, O. Brambles, P. Damiano, M. Wiltberger, and J. Lyon (2012), Magnetotail origins of auroral Alfvénic power, *J. Geophys. Res.*, *117*, A09205, doi:10.1029/2012JA017680.

Zhang, B., O. Brambles, W. Lotko, W. Dunlap-Shohl, R. Smith, M. Wiltberger, and J. Lyon (2013), Predicting the location of polar cusp in the Lyon-Fedder-Mobarry global magnetosphere simulation, *J. Geophys. Res. Space Physics*, *118*, 6327–6337, doi:10.1002/jgra.50565.

Zhang, B., W. Lotko, O. J. Brambles, S. Xi, M. Wiltberger, and J. G. Lyon (2014), Solar wind control of auroral Alfvenic power generated in the magnetotail, *J. Geophys. Res. Space Physics*, *119*, 1734–1748, doi:10.1002/2013JA019178.

Zhang, B., W. Lotko, O. Brambles, M. Wiltberger, and J. Lyon (2015), Electron precipitation models in global magnetosphere simulations, *J. Geophys. Res. Space Physics*, *120*, 1035–1056, doi:10.1002/2014JA020615.

Zhang, B., O. J. Brambles, W. Lotko, J. E. Ouellette, and J. G. Lyon (2016a), The role of ionospheric O^+ outflow in the generation of earthward propagating plasmoids, *J. Geophys. Res. Space Physics*, *121*, 1425–1435, doi:10.1002/2015JA021667.

Zhang, B., O. J. Brambles, M. Wiltberger, W. Lotko, J. E. Ouellette, and J. G. Lyon (2016b), How does mass loading impact local versus global control on dayside reconnection?, *Geophys. Res. Lett.*, *43*, 1837–1844, doi:10.1002/2016GL068005.

Zheng, Y., T. E. Moore, F. S. Mozer, C. T. Russell, and R. J. Strangeway (2005), Polar study of ionospheric ion outflow versus energy input, *J. Geophys. Res.*, *110*, A07210, doi:10.1029/2004JA010995.